Functionalized Mesoporous Silicas Direct Structural Polymorphism of Amyloid-β Fibrils

Michael J. Lucas,[○] Henry S. Pan,[○] Eric J. Verbeke,[○] Lauren J. Webb,* David W. Taylor,* and Benjamin K. Keitz*

Cite This: https://dx.doi.org/10.1021/acs.langmuir.0c00827

Read Online

ACCESS | Metrics & More | Article Recommendations | Supporting Information

ABSTRACT: The aggregation of amyloid-β (Aβ) is associated with the onset of Alzheimer's disease (AD) and involves a complex kinetic pathway as monomers self-assemble into fibrils. A central feature of amyloid fibrils is the existence of multiple structural polymorphs, which complicates the development of disease-relevant structure–function relationships. Developing these relationships requires new methods to control fibril structure. In this work, we evaluated the effect that mesoporous silicas (SBA-15) functionalized with hydrophobic (SBA-PFDTS) and hydrophilic groups (SBA-PEG) have on the aggregation kinetics and resulting structure of Aβ_{1-40} fibrils. The hydrophilic SBA-PEG had little effect on amyloid kinetics, while as-synthesized and hydrophobic SBA-PFDTS accelerated aggregation kinetics. Subsequently, we quantified the relative population of fibril structures formed in the presence of each material using electron microscopy. Fibrils formed from Aβ_{1-40} exposed to SBA-PEG were structurally similar to control fibrils. In contrast, Aβ_{1-40} incubated with SBA-15 or SBA-PFDTS formed fibrils with shorter crossover distances that were more structurally representative of fibrils found in AD patient derived samples. Overall, our results suggest that mesoporous silicas and other exogenous materials are promising scaffolds for the *de novo* production of specific fibril polymorphs of Aβ_{1-40} and other amyloidogenic proteins.
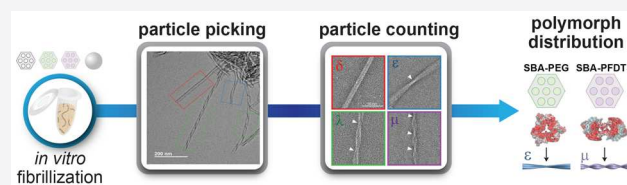
INTRODUCTION

The aggregation of amyloidogenic proteins is associated with a number of neurodegenerative diseases, including Alzheimer's disease (AD).[1−3] Specifically, amyloid-β (Aβ) aggregates and neurofibrillary tangles of tau are implicated in the progression of AD.[4,5] A key challenge in unraveling the pathology of AD and designing effective therapeutics is the paucity of structure–function relationships for amyloid oligomers and fibrils. Unfortunately, the development of such relationships is complicated by the presence of multiple protein isoforms,[6] post-translational modifications,[7−9] and the range of potential fibril structures.[10]

A central feature of amyloid fibrils is structural polymorphism.[11] Fibril polymorphs differ in the registry, orientation (head-to-head versus head-to-tail), and facial symmetry of the protein subunits. Consequently, a vast array of structures are theoretically possible.[10] The structural differences between amyloid fibrils are important because each fibril polymorph potentially exhibits distinct disease and other amyloid-controlled phenotypes.[12−16] For example, the structural heterogeneity of Aβ fibrils may contribute to different AD subtypes and complicates therapeutic development.[17] Thus, the structural characterization of different amyloid fibril polymorphs and an improved understanding of the conditions controlling their structure and biological role are critical steps in evaluating their influence on disease progression.

Among *in vitro* fibrils assembled from a single protein (e.g., Aβ_{1-40}), a number of fibril polymorphs have been structurally characterized using X-ray crystallography, NMR spectroscopy, and electron microscopy (EM).[18−22] Additionally, recent electron microscopy studies have characterized specific fibril polymorphs of α-synuclein, tau, and Aβ from Parkinson's, various tauopathies, and AD patients.[23−25] One consistent finding from these studies was the presence of multiple structural polymorphs among *ex vivo* amyloid fibrils. More importantly, several studies have shown that Aβ fibrils prepared *in vitro* are structurally distinct from Aβ fibrils isolated from AD patients.[24,26] Specifically, *ex vivo* fibrils displayed right-handed twists with hydrophobic residues exposed to solvent, while fibrils formed *in vitro* exhibited left-handed twists with a hydrophobic core.[24] Given these differences, it is unclear what percentage of theoretical fibril structures are accessible *in vivo* or how aggregation conditions influence fibril structure.[27−29] Overall, there is a pressing need for methods that enable the production or isolation of specific

amyloid polymorphs as well as imaging techniques that can characterize heterogeneous populations of fibril structures.

Amyloid formation is a nucleation-driven process heavily influenced by the surrounding environment.[30−33] For example, a variety of environmental stimuli, including metal ions, chaperones, membranes, and other cellular machinery, strongly impact amyloid formation.[34−39] Although amyloid nucleation and growth is very complex, classical nucleation theory predicts that the environment of the critical nucleus should influence the structure of the resulting aggregate (Figure 1a).[40−42]
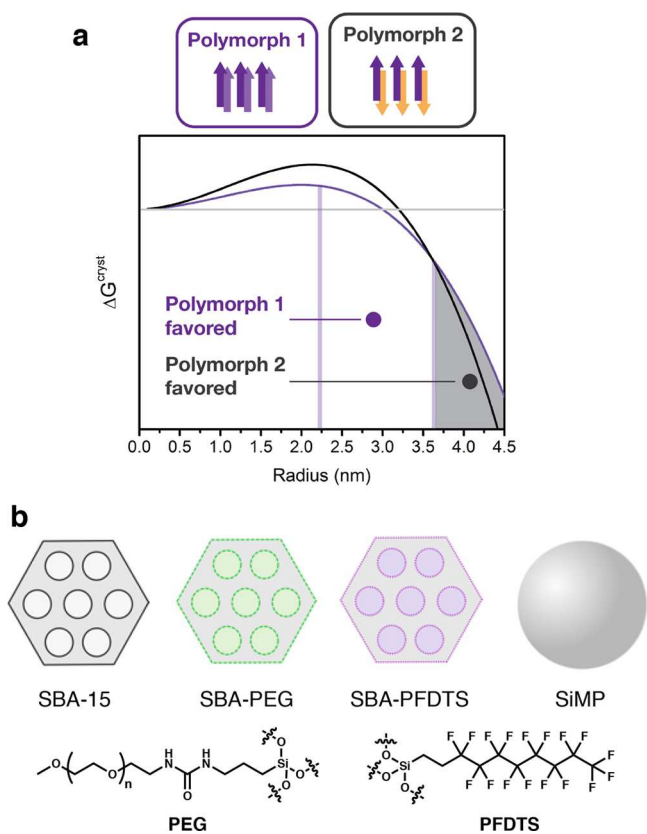

Figure 1. (a) Classical nucleation theory applied to the aggregation of Aβ. The critical nucleus is determined by the balance of bulk (volume) and interfacial forces. These forces ultimately determine the thermodynamic favorability of one polymorph over another. (b) The materials used in this study and the respective functional groups of SBA-PFDTS and SBA-PEG.

Nucleation theory is widely applied to direct the crystallization of small molecule polymorphs, and nucleation-driven control over amyloid structure has been used to produce fibrils of sufficient purity for X-ray crystallography and solid-state NMR spectroscopy through repeated seeding.[19,43] Additionally, amyloid seeds (tau) from brain extract faithfully reproduce conformational features in tau fibrils formed from recombinant protein.[44] In addition to amyloid seeds, prior work has shown that exogenous materials, including nanoparticles, polymers, and small molecules, can act as nucleants that influence the kinetics of amyloid aggregation.[45−49] While the effect of these agents on the kinetics of amyloid formation has been widely studied, it is generally unclear how changing aggregation conditions dictates the structure of the resulting amyloid fibrils. Given these prior results and the potential influence over the nucleation step, we hypothesized that exogenous materials

could affect the structure of Aβ fibrils and potentially direct the formation of specific fibril polymorphs.

Here, we demonstrate that Aβ_{1-40} incubated with surface-functionalized mesoporous silicas (SBA-15) produces distinct amyloid fibril polymorph populations that depend on the silica surface chemistry. We characterized the interaction between the silicas and Aβ_{1-40} using a variety of techniques including fluorescence spectroscopy, IR spectroscopy, and atomic force microscopy. Subsequently, we used negative-stain EM to identify different fibril polymorphs, which were defined by the number of twists, or crossover features, per length of fibril. Using EM, we quantified relative fibril polymorph populations after Aβ_{1-40} was incubated with each material and found that the presence of specific fibril structures was highly dependent on silica surface chemistry and porosity. Specifically, SBA-15 and hydrophobically functionalized SBA-15 accelerated Aβ_{1-40} aggregation kinetics and resulted in a higher population of fibrils with a shorter crossover distance. Notably, Aβ_{1-40} fibrils with this feature are more structurally consistent with the structures of *ex vivo* fibrils. In contrast, buffer controls and hydrophilically functionalized SBA-15 formed fibrils with either no crossover or a 120 nm crossover distance. By evaluating the combined effects of porosity, surface chemistry, surface area, and surface charge on the structure of populations of amyloid fibrils, our results suggest that synthetic materials can be leveraged for the *de novo* production of specific amyloid fibril populations and reinforce the use of negative-stain EM for the rapid characterization of heterogeneous populations of fibril polymorphs.

■ EXPERIMENTAL SECTION

SBA-15 Synthesis. A 4 g sample of Pluronic 123 (M_n 5800, Sigma-Aldrich no. 435465) was mixed with 30 mL of H_2O and 70 mL of 2 M HCl for 1 h at room temperature. The mixture was then brought to 40 °C and 9 g of tetraethyl orthosilicate (98%, ACROS Organics no. 1577812500) was added. The reaction mixture was stirred for 24 h and then vacuum filtrated. The resulting product was aged in an oven at 100 °C for an additional 24 h. To remove residual surfactant from the pores, samples were calcined at 600 °C for 8 h.

SBA-15 Functionalization. A 500 mg sample of SBA-15 was mixed with 110 mg of 1*H*,1*H*,2*H*,2*H*-perfluorododecyltrichlorosilane (PFDTS; Sigma-Aldrich no. 729965) or 160 mg of mPEG-silane (M_n 1000, Laysan Bio Inc.) in 35 mL of dry toluene in a nitrogen atmosphere. The reaction was then carried out under an argon atmosphere at 110 °C under reflux for 20 h. The resulting product was then vacuum filtrated and dried under high vacuum on a Schlenk line.

Surface Area Measurements. Using an ASAP 2020 Physisorption (Micromeritics), the BET surface area was measured for the various mesoporous silicas, using He gas for free space measurements and N_2 gas for adsorption. Samples were activated at 120 °C under high vacuum (10 μbar) for 24 h prior to the BET measurement.

Zeta (ζ) Potential Measurements. Using a dynamic light scattering Zetasizer (Malvern 2010), the ζ potential was measured using a suspended mixture of mesoporous silica (0.25 mg/mL) in 10 mM sodium phosphate (NaPi) buffer at 25 °C. ζ potentials are represented as the average of triplicates, each with 20 minimum scans.

NMR of Functionalized SBA. Functionalization of the SBA-15 was confirmed using an AVANCE III 400 solid-state NMR, running ^{13}C NMR at a spin of 8 kHz. Resulting spectra were evaluated using MestreNova.

Preparation of Aβ_{1-40}. A 5 mg sample of Aβ_{1-40} (BACHEM, H-1994) was dissolved in 500 μL of hexafluoro-2-propanol (HFIP) and shaken at 300 rpm for 1 h. An additional 500 μL of HFIP was added, and 40 μL aliquots were distributed into microcentrifuge tubes. The

HFIP was allowed to evaporate overnight and subsequently dried using a vacuum centrifuge. The samples were stored at −20 °C.

Kinetic Assays of Aβ_{1-40} Aggregation. An aliquot of monomer (230 μg) was thawed and then dissolved in 20 μL of DMSO and 880 μL of 10 mM sodium phosphate (NaPi) buffer to produce a 60 μM solution of Aβ_{1-40}. Aliquots of dissolved monomer (100 μL) were then pipetted into a nonbinding, coated 96 well plate (Corning 3991). Each well was then diluted with 100 μL of a suspension containing 0.5 mg mL^{-1} exogenous material and 200 μM thioflavin T (ThT) in 10 mM NaPi. The final volume of each well was 200 μL with a concentration of 30 μM Aβ_{1-40}, 100 μM ThT, and 0.25 mg mL^{-1} exogenous material in 10 mM NaPi. The 96 well plate was sealed with spectroscopy grade tape (Thermo Scientific no. 235307) and placed in a plate reader (Clariostar, BMG Labtech) at 37 °C. Assays were conducted with shaking at 300 rpm. ThT fluorescence intensity was measured with an excitation of 440 nm and an emission of 480 nm through the top of the plate. Measurements were taken every 300 s for 20 h. Each sample was run in triplicate with blanks (without Aβ_{1-40}) to account for ThT interactions with the exogenous material.

Lag Time Calculations. The lag time for each kinetic assay was calculated by fitting a sigmoidal curve to the fluorescence data of the aggregation (eq 1)

$$F(t) = F_o + \frac{A}{1 + \exp(-k(t - t_{1/2}))} \tag{1}$$

where A is the amplitude of the largest fluorescence intensity, F_o is the background fluorescence, and $t_{1/2}$ is the time at which the intensity is 1/2 of the maximum value.[8] The lag time, t_{lag}, is defined as the intercept of the tangent line at $t_{1/2}$ with slope k (eq 2):

$$t_{lag} = t_{1/2} - \frac{2}{k} \tag{2}$$

Binding Affinity Bradford Assay. To evaluate the binding affinity of Aβ_{1-40} for the surface and pores of the nanoparticles, a 200 μL solution of 30 μM Aβ was mixed with the various materials ranging in concentration from 0.1 to 15 mg mL^{-1} in a microcentrifuge tube. These suspensions were incubated for 15 min at room temperature, shaking at 300 rpm. The samples were subsequently centrifuged, and 20 μL of the supernatant was added to 180 μL of Coomassie Plus (Thermo Scientific no. 23238). Absorbance measurements were taken at 595 nm in triplicate, and the absorbance intensity was then compared to a calibration curve to determine the protein concentration of the supernatant. Association constants were calculated by modeling the absorption curve to a Langmuir isotherm.

Binding Affinity Western Blot Assay. Aβ_{1-40} monomer, 30 μM, was incubated for 20 h at 4 °C to form oligomers. The preformed oligomers were then incubated with each material (0.25 mg mL^{-1}) for 15 min at room temperature in a 1.5 mL microcentrifuge tube, and the suspension was subsequently centrifuged. The supernatant was then collected and photo-cross-linked using the PICUP reaction.[50] An 18 μL volume of the supernatant was mixed with 1 μL of 3 mM tris(2,2′-bipyridyl)dichlororuthenium(II) and 1 μL of 60 mM ammonium persulfate in a 0.2 mL PCR tube. The mixture was irradiated with an LED light for 10 s and quenched with 20 μL of a 5% solution of β-mercaptoethanol. Samples were prepared for SDS-PAGE, by the addition of dye and then heating at 95 °C for 7 min. After SDS-PAGE, the gel was transferred to a 0.2 μm PVDF membrane and blocked in 4% milk. The membrane was then incubated with 6E10 (1:1000) and goat antimouse HRP (1:2500).

Atomic Force Microscopy. Samples were prepared by centrifuge-spinning the incubated Aβ from the different types of functionalized mesoporous silica, at 15,000 rpm for 2 min. After separation of the Aβ-containing supernatant from the mesoporous silica pellet, a 100 μL aliquot was deposited onto a piece of freshly cleaved mica (Ted Pella, highest grade mica sheets) and incubated at room temperature for 1 min. The excess liquid was then removed from the edge of the mica with a Kimwipe, and the surface was rinsed with a 100 μL aliquot of Dulbecco's phosphate buffered saline (Sigma) before it was dried under a stream of N$_2$(g). An Asylum MFP-3D atomic force

microscope was used to image drop-cast Aβ on freshly cleaved mica. AFM cantilevers (MikroMasch) with a typical probe radius of 8 nm, 65 kHz resonance frequency, and 0.5 N m^{-1} force constant were used to analyze the surface under tapping mode, to minimize sample damage due to shear forces and tip−sample interactions. All images were processed using the Gwyddion SPM software package.

Attenuated Total Reflectance Infrared Spectroscopy (ATR-IR). Vibrational spectra were collected with a Bruker Vertex 70 Fourier transform infrared (FTIR) spectrometer equipped with a VeeMAX II ATR accessory (Bruker) to illuminate the sample. The samples were centrifuged at 21,000 rcf for 2 min to concentrate the Aβ suspension. With the use of a centrifugal evaporator to remove the liquid, the Aβ was then resuspended in 10 μL of 10 mM sodium phosphate buffer (NaPi) of pH 7.4 to a concentration of 2 mM and deposited onto a ZnSe ATR crystal. After the sample chamber was purged with N$_2$(g) for 30 min, 500 scans of light were collected from each sample. A mercury cadmium telluride (MCT) detector was used to collect signals from 800 to 3000 cm^{-1}. For each sample, a background sample of supernatant from an incubation using only mesoporous silica was prepared identically to the process described above in order to determine the absolute difference of absorption due to Aβ. Following this background subtraction, spectra were flattened using a rubber band correction baseline function in the instrument's OPUS software.

Transmission Electron Microscopy. Transmission electron microscopy was used to analyze the morphology of the mesoporous silica and the resulting Aβ_{1-40} fibrils. Samples were prepared on carbon coated grids (Electron Microscopy Sciences, CF400) that were glow discharged with an EmiTech K100x Coater. After the amyloid samples were allowed to aggregate for 24 h, 7 μL of the amyloid−mesoporous silica suspension was drop-cast on the charged carbon side of the grid. After incubating for 1 min, the droplets were washed two times each with in 50 μL of 0.1 and 0.01 M ammonium acetate. The droplet was then washed with 50 μL of 2% uranyl acetate. Following the washes, excess liquid was wicked away using filter paper. Negative-stain images were acquired on a JEOL 2010F TEM operated at 200 kV at a nominal magnification of 60000×, which resulted in a pixel size of 3.6 Å/pixel. The exposure for each image was 2 s, resulting in a total electron dose of 60−70 e$^-$ Å^{-2}. Data was collected on a Gatan OneView camera with a defocus ranging from −0.5 to −4.0 μm.

Image Processing. Fibril segments were picked using eman2he-lixboxer from the EMAN2 image processing suite,[51] with a box size of 344 pixels (120 nm) and no overlap. This box size was selected based on the measurement of the longest helical crossover distance observed. Fibril particles initially were manually picked using EMAN2 from 100 micrographs of each of six incubation conditions which were then extracted and segmented into particles with a box size of 1238.4 Å using RELION. Approximately 520 particles were used to measure the distributions of fibrils with different helical crossover distances across conditions. The particles were further refined by 2D classification into three classes using RELION with helical symmetry optimization enabled. Additional replicates were each comprised of 20 micrographs for each condition and processed using the same workflow described above.

Statistical Analysis. Unless otherwise noted, data are reported as mean ± SD of $n = 3$ biological replicates. Significance was calculated in GraphPad Prism 8.0 using either a two-tailed unpaired Student t test or a one-way ANOVA ($\alpha = 0.05$).

■ RESULTS AND DISCUSSION

To probe the effect of exogenous materials on Aβ_{1-40} fibril polymorphism, we initially examined Santa Barbara Amorphous-15 (SBA-15), which is synthesized in a cooperative self-assembly process using a triblock copolymer consisting of ethylene oxide and propylene oxide units as a template followed by the addition of a silica source.[52] The resulting mesoporous structure contains large cylindrical pores (4−30 nm), high surface area (>1000 m^2 g^{-1}), and tunable surface

chemistry.[53] These attributes are important because previous studies have shown that porosity and confinement influence nucleation and direct the resulting structure of small molecule crystals by changing the critical nucleation radius.[54,55] Moreover, SBA-15 has been shown to confine both myoglobin and lysozyme within its porous network, acting as an artificial chaperone that can affect protein structure.[56,57] In addition to leveraging its porosity and high surface area, many applications using SBA-15 require surface functionalization through postsynthetic grafting of organosilanes.[58] Thus, we envisioned that the tunable surface chemistry of SBA-15 would allow us to tailor its interactions with $A\beta_{1-40}$ and investigate how changes in the chemical and structural environment of the monomeric protein affect its aggregation into a three-dimensional fibril structure.

Following SBA-15 synthesis, we used organosilane grafting to functionalize the material with a hydrophobic group, perfluorododecyltrichlorosilane (PFDTS), and hydrophilic group, polyethylene glycol (PEG) (Figure 1b). These functional groups were selected to evaluate the combined effects of surface charge, surface area, and hydrophobicity on $A\beta_{1-40}$ aggregation kinetics and fibril structure. Finally, we also examined silica microspheres (SiMP; Cospheric SiO2MS-2.0 0.507 μm) with a diameter of 500 nm as a control material to evaluate the effect of porosity on $A\beta_{1-40}$ aggregation and fibril structure. Following synthesis and postsynthetic modifications, all materials were analyzed for surface area, surface charge, morphology, and surface chemistry (Table S1, Figures S1–S3). Overall, using thermogravimetric analysis and NMR spectroscopy, we confirmed that surface grafting of the hydrophobic and hydrophilic groups was successful. Additionally, physisorption studies revealed that SBA-15 and SBA-PFDTS had the largest surface areas, while SBA-PEG had a reduced surface area available for adsorption.

Aβ Binding Affinity to Mesoporous Silicas. Aβ binds to various proteins, metal ions, and cell receptors.[59−61] Previous investigations have also examined the binding affinity of Aβ to exogenous materials, such as lipid vesicles.[62] Because binding may influence effective protein concentration and structure, we first measured the binding affinity of $A\beta_{1-40}$ to SBA-15 and its variants. Previous studies have shown that protein adsorption to SBA-15 can be modeled using a Langmuir adsorption model.[56] Therefore, using a Bradford assay, we estimated the dissociation constant between monomeric $A\beta_{1-40}$ and our SBA-15 variants. Both SBA-15 and SBA-PFDTS exhibited a relatively high affinity for $A\beta_{1-40}$, with dissociation constants of 235 ± 27 and 112 ± 34 μM, respectively (Figure S4). The 2-fold higher affinity for SBA-PFDTS is most likely a result of its hydrophobic nature and nonspecific binding with the hydrophobic C-terminus of the $A\beta_{1-40}$ monomer.[63] These values are also consistent with previous studies that showed hydrophobic interactions dominated binding between short peptides and amyloids.[64] While $A\beta_{1-40}$ monomers and oligomers are smaller than the pore diameter of SBA-15, we could not verify incorporation of protein in the pores.

In contrast, there was no measurable protein adsorption between $A\beta_{1-40}$ and SBA-PEG and SiMP. The higher molecular weight of the PEG surface functionality reduced the surface area of SBA-PEG (Table S1) while also creating a hydrophilic surface less prone to interact with $A\beta_{1-40}$. We measured a significantly lower surface area for the SiMP (6 m^2 g^{-1}), which potentially explains its lower affinity for $A\beta_{1-40}$.

Overall, these results confirm that surface functionality strongly influences the interaction of SBA-15 with $A\beta_{1-40}$.

Next, we qualitatively validated our $A\beta_{1-40}$ binding affinity measurements to the various materials through Western blot (Figure S5). A mixture of $A\beta_{1-40}$ monomer and preformed oligomers were incubated with each material for 15 min, followed by centrifugation, photo-cross-linking, and SDS-PAGE. As expected, SBA-15 and SBA-PFDTS showed minimal $A\beta_{1-40}$ monomer, oligomer, or fibril bands, indicating these materials effectively adsorbed and pulled down the monomeric protein and aggregates. In contrast, SBA-PEG displayed bands consistent with the $A\beta_{1-40}$ control, suggesting minimal protein interaction with this material. Together, these results confirm that SBA-15 and SBA-PFDTS exhibit strong interactions with both $A\beta_{1-40}$ monomers and aggregates.

Kinetic effects of Mesoporous Silica on $A\beta_{1-40}$ Aggregation. As mentioned above, a variety of environmental factors including exogenous materials, small molecules, and metal ions can influence the fibrillization kinetics of $A\beta_{1-40}$. To determine the specific effect of our materials on the rate of $A\beta_{1-40}$ aggregation, kinetic assays were conducted using thioflavin T (ThT) fluorescence, which is enhanced and red-shifted in the presence of amyloid fibrils.[65] Monomeric $A\beta_{1-40}$ was incubated with each of the exogeneous materials in the presence of ThT, and fluorescence spectra were collected for up to 20 h (Figure S6). For the first 5 h of incubation, no fluorescence was measured from any solution, indicating monomer association and dissociation in the absence of fibril formation (Figure 2).[66] Each solution then went through a
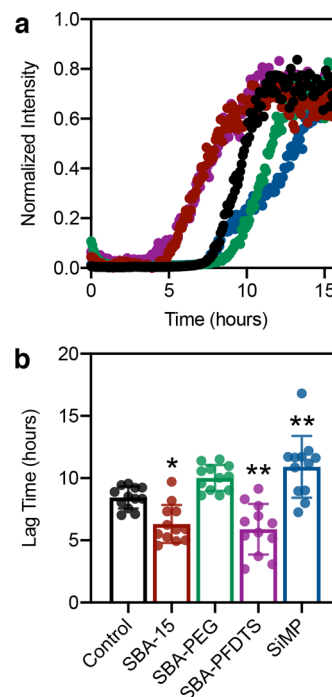

Figure 2. (a) Raw kinetic curves of the aggregation of 30 μM $A\beta_{1-40}$ in 10 mM NaPi (black) at 37 °C and in the presence of 0.25 mg mL^{-1} SBA-15 (red), SBA-PEG (green), SBA-PFDTS (purple), and SiMP (blue). (b) Calculated lag time of aggregation. Fibrillization is accelerated in the presence of SBA and SBA-PFDTS. Error bars represent one standard deviation ($n = 12$). *, $p < 0.05$; **, $p < 0.01$, using a one-way ANOVA. Replicate kinetic data is presented in Figure S6.
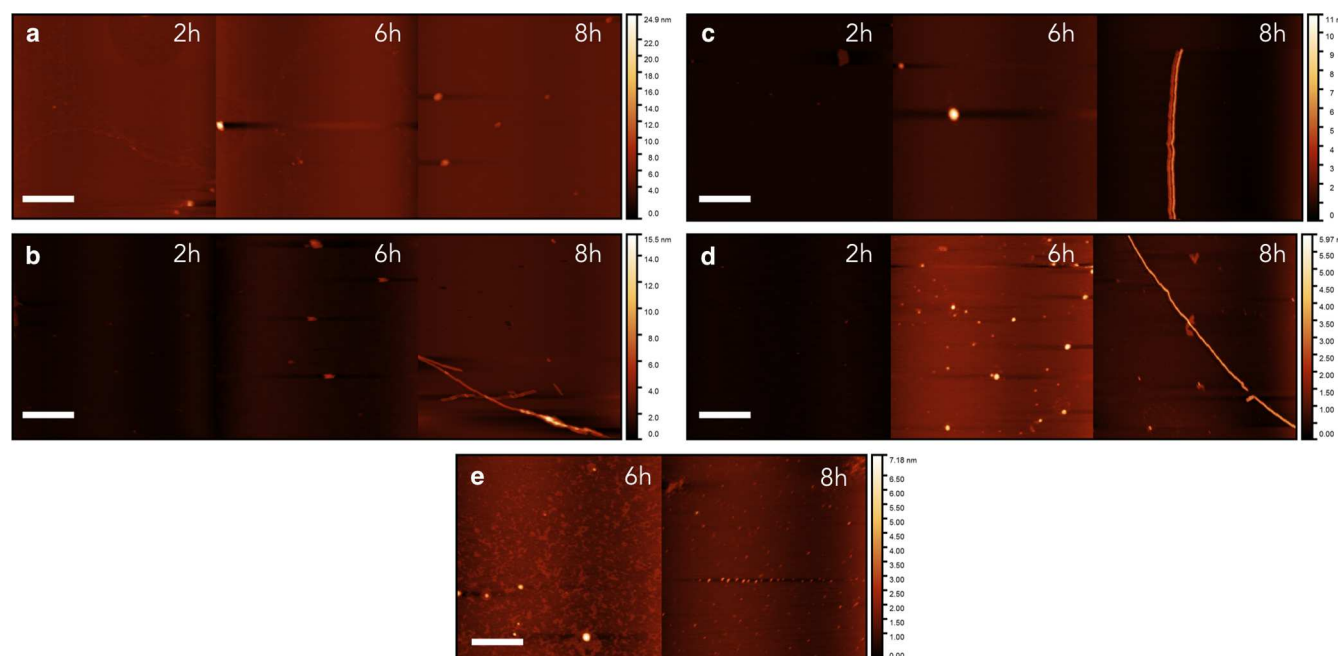
Figure 3. AFM images of 30 μM Aβ_{1-40} after incubation in (a) 10 mM NaPi and 0.25 mg mL^{-1} (b) SBA-15, (c) SBA-PEG, (d) SBA-PFDTS, and (e) SiMP at 37 °C after 2, 6, and 8 h. Note that no oligomers were detected for SiMP at 2 h. Scale bars are 500 nm. Images collected after 24 h can be found in the Supporting Information.

rapid increase in ThT fluorescence, indicating rapid growth of mature fibrils due to fibril-catalyzed secondary nucleation.[33] The length of the lag phase can be quantitatively estimated by modeling the fluorescence curves with a sigmoid function and evaluating the intercept of the tangent line at $t_{1/2}$.[67] Upon analysis of the lag time, we found that both porosity and surface chemistry influenced the aggregation kinetics of Aβ_{1-40}. As seen in Figure 2, SBA-15 and SBA-PFDTS accelerated aggregation kinetics as indicated by a reduction in the length of the lag phase. Conversely, SiMP slightly slowed aggregation kinetics by extending the length of the lag phase, while SBA-PEG had no discernible effect, relative to the control, on the fibrillization rate. The rapid aggregation of Aβ_{1-40} in the presence of hydrophobic surfaces is consistent with previous studies, which found that these surfaces enhance *in vitro* and *in vivo* fibril self-assembly of Aβ_{1-40} and other amyloidogenic proteins.[68,69]

Preliminary Structural Effects of Mesoporous Silicas on Aβ_{1-40} Fibrils. Next, we investigated the effect of the silica materials on the structure of Aβ_{1-40} fibrils. First, infrared spectroscopy was used to determine if the β-sheets within the cross-β motif of the fibril were parallel or antiparallel. Previous studies have shown that Aβ fibrils are largely comprised of in-register parallel sheets.[70] However, antiparallel sheets have been found in fibrils formed by smaller Aβ fragments and in amyloid-like crystals.[70,71] Both parallel and antiparallel sheets have shown cytotoxic behavior, but the different arrangement of peptides into sheets could indicate different mechanisms of aggregation and self-assembly.[70] Our IR measurements of the fibrils formed in the presence of the various materials led to a single peak at 1650 cm^{-1} (Figure S7), suggesting that parallel β-sheets were formed under all conditions tested.

To further probe the structural effects of mesoporous silicas on Aβ_{1-40}, atomic force microscopy (AFM) was used to image the aggregates at various times in the fibrillization process. Relative to fluorescence measurements, AFM offers the

advantage of being able to detect oligomers and smaller aggregates on the nanoscale that cannot be detected by other spectroscopic and microscopic methods.[72] In order to examine the various aggregates using AFM, Aβ_{1-40} was incubated with SBA-15, SBA-PFDTS, SBA-PEG, and SiMP. Aliquots of the supernatant were taken at 2, 6, 8, and 24 h to capture a variety of states of the aggregation process, and are shown in Figure 3. The SBA-15 and SBA-PFDTS trials both exhibited fibril formation at 8 h when compared to the control, indicating an acceleration in the kinetics. Conversely, SiMP inhibited fibril formation, with only small aggregates detected by AFM after 24 h of observation (Figure S8). The inhibition of fibril formation in the presence of SiMP was demonstrated by the increased lag time in the ThT assays (Figure 3b); however, we were unable to visualize any fibrils from this condition on AFM. We attribute this to a decrease in the total population of fibrils formed in the presence of SiMP. Ultimately, using AFM, we validated the kinetic trends observed in our ThT fluorescence experiments and confirmed that the Aβ_{1-40} behaves differently in the presence of the silicas with varying surface chemistry.

Effect of Mesoporous Silicas on Fibril Polymorph Distribution. While IR and AFM provide basic insights into the structure and growth dynamics of amyloid fibrils,[73] transmission electron microscopy can reveal the morphology and helical crossover distance of fibril structures. Additionally, EM provides an advantage over other structural methods by capturing a large field of individual fibrils in a single image that do not need to be purified to homogeneity. For example, previous EM studies revealed that Aβ_{1-40} fibrils take on various structures and the distribution of these polymorphs can change depending on the fibrillization conditions.[27,74,75] Thus, we used negative-stain EM to rapidly discern and quantify specific Aβ_{1-40} polymorphs formed in the presence of each exogenous material. While cryo-EM has been used to obtain atomic resolution structures of *ex vivo* Aβ, tau, and α-synuclein fibrils,
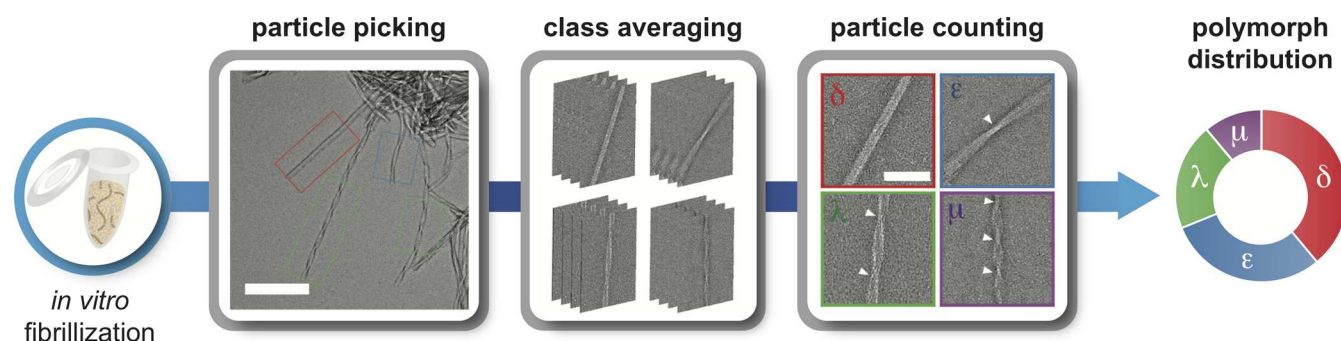
Figure 4. Workflow of the acquisition of fibril polymorph distributions. Aβ_{1-40} was incubated with each material for 24 h at 37 °C. Fibrils were drop-cast on TEM grids and stained for imaging. Particles displaying various morphologies were picked with a box size of 123.84 nm. The various morphologies were split into four classes based on crossover distances of 0 (δ), 40 (μ), 60 (λ), and 120 nm (ε). Particles were then counted and used to calculate the overall polymorph distribution in each condition. Scale bars are 200 nm for particle picking and 50 nm for particle counting.

we chose to use negative-stain EM as samples were easily prepared and it offers a higher signal-to-noise ratio.

To determine the effect of our materials on fibril polymorphism, Aβ_{1-40} monomer was incubated with each material for 24 h. Each fibrillization experiment was conducted in triplicate to determine the reproducibility of morphological distributions formed in the presence of each exogenous material. Following incubation, fibril samples were collected by centrifugation, drop-cast onto EM grids, and stained with uranyl acetate, U(OAc)$_2$. Nonoverlapping particles and particles distanced from silica materials were selected from micrographs in order to accurately measure the population frequency of fibrils that adopted a specific crossover distance. We then performed reference-free 2D classification using RELION[76] to investigate the structural similarity of Aβ_{1-40} morphologies observed across each condition (Figure 4). The 2D class averages confirmed the internal consistency of structure within each fibril and external consistency between fibrils formed under different conditions (Figure S9). Across the entire sample set, fibrils with no crossover or crossover distances of 120, 60, and 40 nm were observed for Aβ_{1-40}. To the best of our knowledge, there is no standard nomenclature for different Aβ_{1-40} fibril polymorphs; therefore, we labeled the observed fibrils as δ, ε, λ, and μ fibrils, respectively. Consistent with previous studies, fibrils that markedly changed helical crossover distance along different parts of the length were very rarely observed (ca. 0.1%).[16] Overall, the observed structures derived from class averaging agree with previous studies investigating the structural polymorphism of Aβ_{1-40} fibrils.[27]

In the Aβ control and SBA-PEG conditions, we observed primarily δ fibrils (no crossover), ε fibrils (120 nm crossover distance), and a small population of λ fibrils (60 nm crossover distance). Specifically, the Aβ control produced 20.5 ± 9.2% δ fibrils, 72.5 ± 13.6% ε fibrils, and 7.1 ± 6.3% λ fibrils. This was comparable to the SBA-PEG, which produced 24.1 ± 17.5% δ fibrils, 71.6 ± 22.2% ε fibrils, and 4.3 ± 4.9% λ fibrils. Notably, these values are also consistent with previous literature reports describing the structure of fibrils formed under comparable conditions.[75] With SBA-15, we observed a decrease in the percentage of ε fibrils at 32.1 ± 9.1%, which was offset by an increase of δ and λ fibrils at 38.9 ± 16.6 and 23.5 ± 13.6%, respectively, as well the appearance of a small population of μ fibrils (40 nm crossover distance), at 5.5 ± 7.9%.

SBA-PFDTS produced a distribution of fibrils that was significantly different from all other material conditions. Specifically, there was a large increase in the percentage of λ

fibrils compared to the rest of the conditions, where 49.0 ± 10.3% λ fibrils were present. The polymorph distributions displayed in both the SBA-15 and SBA-PFDTS conditions, with an overall decrease in crossover distance, were the most consistent to that of fibrils obtained *ex vivo*, albeit with the opposite helicity.[24] Finally, the SiMP produced a population similar to the control, with a small population of μ fibrils observed, indicating the potential importance of porosity and surface area in the nucleation process.

Because both SBA-15 and SBA-PFDTS accelerated the kinetics of amyloid formation, we next examined whether their unique fibril population distributions were the result of a purely kinetic effect. For example, we asked if alternative incubation conditions that also accelerate fibril formation result in a similar polymorph distribution to SBA-PFDTS. To test this, Aβ_{1-40} monomer was incubated with sodium dodecyl sulfate (SDS), which is known to accelerate the aggregation of Aβ.[77] As expected, SDS accelerated fibrillization kinetics with a comparable lag time to SBA-PFDTS (Figure S11). However, as seen in Figure 5, SDS produced a population of fibrils distinct from that of SBA-PFDTS, indicating that the observed fibril populations are the result of material effects beyond the rate of aggregation.

Discussion. We demonstrated that changing the surface area and functionalization of mesoporous silicas impacted the aggregation kinetics and structure of Aβ_{1-40} fibrils. In the case of ThT assays, we found that the addition of materials with differing surface chemistries altered the aggregation kinetics of fibril formation. Accelerated kinetics and a shorter lag phase were observed when Aβ_{1-40} was incubated with SBA-15 and SBA-PFDTS. In contrast, no significant changes in aggregation kinetics or the length of the lag phase were observed when Aβ_{1-40} was incubated with SBA-PEG. We attribute these accelerated kinetics in SBA-15 and SBA-PFDTS to the high surface area of SBA-15 (886 m^2/g) and the additional hydrophobicity of SBA-PFDTS.[68,69] In contrast, the relative hydrophilicity of the SBA-PEG mitigated any acceleration effects, yielding a lag time similar to that of the Aβ_{1-40} control. For comparison, we also tested the effect of SiMPs, which have a comparable particle diameter to the SBA-15 variants but a lower surface area (6 m^2/g). We hypothesize that the lower surface area of the SiMPs is responsible for their negligible effect on amyloid kinetics. To confirm these results, we also conducted AFM measurements to visualize Aβ_{1-40} oligomers and fibrils across a 24 h period. The AFM results were consistent with the aggregation kinetics observed in the ThT
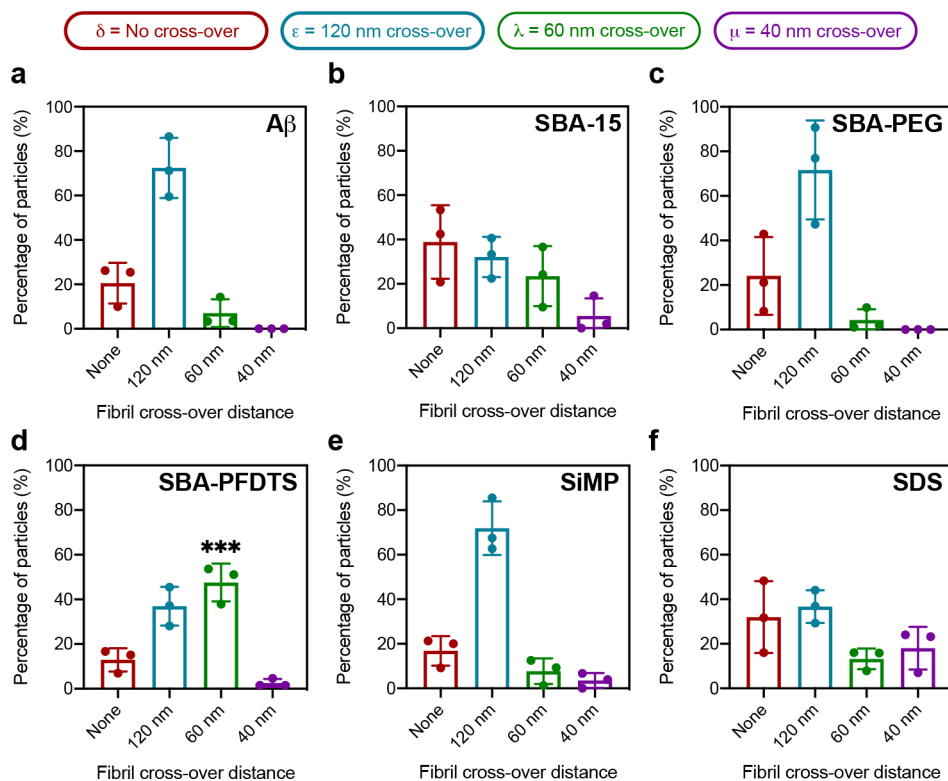
Figure 5. Distributions of crossover distance in $A\beta_{1-40}$ fibrils after a 24 h incubation with (a) 10 mM NaPi buffer and 0.25 mg mL^{-1} (b) SBA-15, (c) SBA-PEG, (d) SBA-PFDTS, (e) and SiMP. To test if these distributions were truly the result of a material effect rather than accelerated kinetics, distributions were also measured in the presence of (f) 100 μM SDS. Population fractions of each polymorph were averaged over three biological replicates (independent fibrillization experiments), and error bars represent one standard deviation. SBA-PFDTS produced a λ population significantly different from the control. ∗∗∗, p = 0.0002 using one-way ANOVA.

assays (Figure 3). Overall, our kinetic and biophysical studies agree with previous reports examining the effect of exogenous materials and hydrophobic interfaces on the aggregation kinetics of amyloid formation, while providing additional insight into the effect of porosity, surface area, and surface chemistry on amyloid fibrillization.

Nucleation theory and amyloid specific work have suggested that influencing the nucleation environment can potentially control the distribution of fibril structures.[74,78] To test this hypothesis, we analyzed the population distribution of different fibril polymorphs formed in the presence of functionalized mesoporous silicas using negative-stain EM and 2D classi-fication. The use of negative-stain EM, instead of cryo-EM, for quantifying fibril populations offered a relatively high throughput method for imaging and visualizing structural differences across incubation conditions, which allowed us to test a variety of nucleation environments in a statistically significant manner. To rapidly classify different polymorphs, we sorted fibril particles based on different crossover distances, since this feature was most distinct when differentiating polymorphs during the class-averaging process. Through this analysis, we observed significant differences in the distribution of amyloid fibril polymorphs for each incubation condition and that changes to the exogenous material's porosity and surface functionalization influenced the frequency of one fibril structure compared to another. Overall, we observed fibrils with no crossover (δ-$A\beta_{1-40}$) and crossover distances of ca. 120 (ε-$A\beta_{1-40}$), 60 (λ-$A\beta_{1-40}$), and 40 nm (μ-$A\beta_{1-40}$).

As shown in Figure 5, $A\beta_{1-40}$ incubated under control conditions and in the presence of SBA-PEG or SiMP primarily produced δ and ε fibrils. Previous reports using EM and solid-state NMR (SSNMR) spectroscopy identified amyloid fibrils with potential similar structures when $A\beta_{1-40}$ was incubated in a variety of simple buffers. The inclusion of different salt ions also produced similar distributions of δ and ε fibrils.[79] The δ fibrils are dimeric in each fibril repeat,[43] while the ε fibrils can contain two to four peptides in each repeat.[19,80] Additionally, the reported atomic resolution structures show that δ fibrils have parallel, in-register β-sheets, consistent with our IR results, with the majority of hydrophobic amino acid side chains residing in the interior of the fibril and the majority of the polar amino acid residues residing on the exterior. Polar zipper interactions may also occur with residue Q15 fitting into the cavity created by Q37 and Q38. A trimeric structure, as shown in Figure 6, has been reported in which each crossover represents a 60° rotation, and is one possible structure of ε fibrils. In this structure, the peptide conformation is similar to that of the δ fibrils, where the majority of the hydrophobic amino acid side chains reside in the core.[19] Overall, the observed dominance of δ and ε fibril structures in our control, SBA-PEG, and SiMP samples is consistent with previous literature reports and validates our methodology for fibril classification.

Consistent with our hypothesis that the nucleation environ-ment can influence fibril structural polymorphism, we observed that SBA-15 and SBA-PFDTS had a unique effect on the distribution of fibril polymorphs. SBA-15 showed a decrease in ε fibrils coupled with an increase of both δ and λ fibrils, as well as the appearance of a population of μ fibrils. SBA-PFDTS
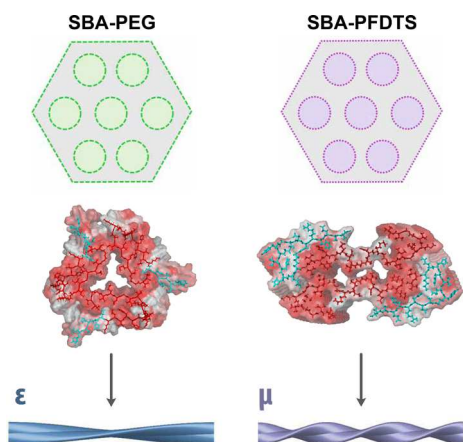
Figure 6. Representative atomic structures of the fibril morphologies observed for SBA-PEG and SBA-PFDTS. Hydrophobic residues are shown in red using color_h in PyMol.[83] ε-Fibrils with a crossover distance of 120 nm (PDB 2LMQ) were primarily observed in the control and in the presence of SBA-PEG. Populations with smaller crossover distances, λ and μ, were observed in the presence of SBA-PFDTS, for which an *ex vivo* fibril with a similar morphology has been observed (PDB 6SHS). In the polymorph with a smaller crossover distance (μ), hydrophobic residues were exposed to the solvent, suggesting that the hydrophobic environment of SBA-PFDTS could be influencing the nucleation.

exhibited a statistically significant increase in the proportion of λ fibrils compared to all other materials tested.

Fibrils with a morphology (crossover distance) similar to our observed μ fibrils were recently identified in an *ex vivo* study involving AD patients, albeit with a helicity opposite to those found in our experiments.[24] These μ fibrils have dimeric fibril repeats, a C-shaped peptide fold, and a central peptide domain that is buried in the fibril core, which interacts between the two peptide stacks at residues 24−26. In contrast to δ and ε fibrils, the majority of charged amino acid side chains in the μ fibril structure are solvent-exposed, and Q11 and K16 are oriented in a manner that can form salt bridges with one another. Small populations of λ fibrils have been observed in previous studies, but the atomic structure has yet to be reported.[80]

Previous molecular dynamics (MD) simulations of fragments of amyloidogenic protein sequences, such as yeast prion-like protein Sup35, have suggested that changes in fibril twisting (crossover distance) may be due to different charge interactions at the protein's N- and C-termini.[81,82] Specifically, with a negative charge at the C-terminus, model proteins adopted the more energetically favorable twisting conformation in MD simulations compared to the fibrils with no crossover distance, which were less energetically favored.[82] These simulation results may explain why the accessible negative surface charge of SBA-15 favors the formation of λ and μ fibrils compared to the ε fibrils that were highly represented in the control, SBA-PEG, and SiMP samples. Similarly, the larger population of λ and μ fibrils observed in the presence of SBA-PFDTS indicates that hydrophobicity plays a significant role in determining fibril structure, and we speculate that hydrophobic environments may generally favor these structures. Analyzing the currently available PDB structures (2LMQ and 6SHS) that could be representative of ε fibrils and μ fibrils revealed that the hydrophobic C-termini in the μ fibril structure are more solvent-exposed than the ε fibrils, as shown in Figure 6.[19,24] Overall, this suggests that the

exposure of different regions of Aβ_{1-40} to the functionalized materials during aggregation determines which polymorph is favored.

It is notable that while SDS accelerated the aggregation kinetics of Aβ_{1-40} and exhibited a moderate increase in the proportion of λ fibrils, the distribution was not as prominent as SBA-PFDTS. This suggests that the increased fraction of λ fibrils observed in the presence of SBA-PFDTS is not solely due to accelerated aggregation, and that the surface area and chemistry of the materials may be the driving mechanism for this morphology. Finally, we hypothesize that the negative charge introduced by the surfactant may have a similar effect on Aβ_{1-40} as SBA-15. Since negative charge can affect structural polymorphism, as seen with tau fibrils,[16] a similar mechanism may be influencing the formation of Aβ_{1-40} in our system, potentially yielding the population of μ fibrils that was not observed in the control and SBA-PEG.

Our main goal was to investigate the effect of mesoporous silicas and influencing nucleation on Aβ_{1-40} fibril polymorphism. As highlighted above, Aβ_{1-40} fibrils adopt a range of structures, even under relatively simple incubation conditions. Different incubation conditions, the use of fibril seeds, the presence of different isoforms, cofactors, and post-translational modifications can all bias the structural distribution of amyloid fibrils. For example, Aβ_{1-42} and Aβ_{1-40} produce distinct *in vitro* fibril structures[75] as does phosphorylated Aβ_{1-40}.[84] Understanding what factors control fibril structure or even what theoretical structures are possible under physiological conditions will be critical to unraveling AD pathology.

The presence of highly heterogeneous Aβ fibril populations may be responsible for different AD subtypes. The observation that different tau isoforms and fibril structures drive distinct tauopathies suggests similar phenomena may occur with Aβ and AD.[16,85] Unfortunately, patient-derived fibrils of both tau and Aβ show significant structural differences compared to their *in vitro* counterparts. Seeding from patient-derived samples can faithfully replicate disease-relevant fibril structures,[44] but these samples are challenging to obtain and this strategy may not be effective for all proteins. Thus, there is a pressing need to develop *in vitro* conditions that recapitulate the features of *ex vivo* fibril structures in order to develop specific hypotheses related to fibril formation and propagation.

■ CONCLUSIONS

Overall, our results show that mesoporous silicas influence the aggregation kinetics of Aβ_{1-40} and the distribution of observed fibril morphologies. By tuning the material properties of mesoporous silicas, we highlighted the potential of exploiting nucleation theory in conjunction with exogenous materials for biasing amyloid formation toward specific fibril polymorph distributions. Future refinement of our methodology could facilitate *in vitro* access to fibril structures more representative of neurodegenerative disease isolates or to specific fibril polymorphs with unique structures and pathologies.

■ ASSOCIATED CONTENT

ⓢ Supporting Information

The Supporting Information is available free of charge at https://pubs.acs.org/doi/10.1021/acs.langmuir.0c00827.

EM of silica materials; TGA of SBA-PEG and SBA-PFDTS; SSNMR of SBA-PEG; binding affinity of Aβ_{1-40}

to SBA-PFDTS and SBA-15; Western blot of $A\beta_{1-40}$ after binding to mesoporous silicas; replicate $A\beta_{1-40}$ kinetic data; FTIR of $A\beta_{1-40}$; AFM of $A\beta_{1-40}$ at 24 h; workflow of TEM class averages of $A\beta_{1-40}$ fibrils; replicate fibril morphology raw counts; kinetics of $A\beta_{1-40}$ in SDS; surface area and surface charge of mesoporous silicas (PDF)

■ AUTHOR INFORMATION

Corresponding Authors

Lauren J. Webb − *Department of Chemistry, University of Texas at Austin, Austin, Texas 78712, United States;* ⊙ orcid.org/0000-0001-9999-5500; Email: lwebb@cm.utexas.edu

David W. Taylor − *Institute for Cellular and Molecular Biology, Department of Molecular Biosciences, and Center for Systems and Synthetic Biology, University of Texas at Austin, Austin, Texas 78712, United States; LIVESTRONG Cancer Institutes, Dell Medical School, Austin, Texas 78712, United States;* ⊙ orcid.org/0000-0002-6198-1194; Email: dtaylor@utexas.edu

Benjamin K. Keitz − *McKetta Department of Chemical Engineering, University of Texas at Austin, Austin, Texas 78712, United States;* ⊙ orcid.org/0000-0003-3314-0053; Email: keitz@utexas.edu

Authors

Michael J. Lucas − *McKetta Department of Chemical Engineering, University of Texas at Austin, Austin, Texas 78712, United States;* ⊙ orcid.org/0000-0003-2564-2416

Henry S. Pan − *McKetta Department of Chemical Engineering, University of Texas at Austin, Austin, Texas 78712, United States*

Eric J. Verbeke − *Institute for Cellular and Molecular Biology, University of Texas at Austin, Austin, Texas 78712, United States*

Complete contact information is available at:
https://pubs.acs.org/10.1021/acs.langmuir.0c00827

Author Contributions

Notes

The authors declare no competing financial interest.

Experimental data supporting the findings in this study are publicly available through the Texas Data Repository at https://doi.org/10.18738/T8/CNVOB6.

■ REFERENCES

(1) Wang, J.; Gu, B. J.; Masters, C. L.; Wang, Y. J. A Systemic View of Alzheimer Disease - Insights from Amyloid-β Metabolism beyond the Brain. *Nat. Rev. Neurol.* **2017**, *13*, 612−623.

(2) Poewe, W.; Seppi, K.; Tanner, C. M.; Halliday, G. M.; Brundin, P.; Volkmann, J.; Schrag, A. E.; Lang, A. E. Parkinson Disease. *Nat. Rev. Disease Primers* **2017**, *3*, 17013.

(3) Banci, L.; Bertini, I.; Boca, M.; Girotto, S.; Martinelli, M.; Valentine, J. S.; Vieru, M. SOD1 and Amyotrophic Lateral Sclerosis: Mutations and Oligomerization. *PLoS One* **2008**, *3* (2), e1677.

(4) Selkoe, D. J.; Hardy, J. The Amyloid Hypothesis of Alzheimer's Disease at 25 Years. *EMBO Mol. Med.* **2016**, *8* (6), 595−608.

(5) Long, J. M.; Holtzman, D. M. Alzheimer Disease: An Update on Pathobiology and Treatment Strategies. *Cell* **2019**, *179*, 312−339.

(6) Wildburger, N. C.; Esparza, T. J.; Leduc, R. D.; Fellers, R. T.; Thomas, P. M.; Cairns, N. J.; Kelleher, N. L.; Bateman, R. J.; Brody, D. L. Diversity of Amyloid-Beta Proteoforms in the Alzheimer's Disease Brain. *Sci. Rep.* **2017**, *7* (1), 9520.

(7) Jawhar, S.; Wirths, O.; Bayer, T. A. Pyroglutamate Amyloid-β ($A\beta$): A Hatchet Man in Alzheimer Disease. *J. Biol. Chem.* **2011**, *286*, 38825−38832.

(8) Schedin-Weiss, S.; Winblad, B.; Tjernberg, L. O. The Role of Protein Glycosylation in Alzheimer Disease. *FEBS J.* **2014**, *281* (1), 46−62.

(9) Chow, V. W.; Mattson, M. P.; Wong, P. C.; Gleichmann, M. An Overview of APP Processing Enzymes and Products. *NeuroMol. Med.* **2010**, *12*, 1−12.

(10) Eisenberg, D. S.; Sawaya, M. R. Structural Studies of Amyloid Proteins at the Molecular Level. *Annu. Rev. Biochem.* **2017**, *86* (1), 69−95.

(11) Colletier, J.-P.; Laganowsky, A.; Landau, M.; Zhao, M.; Soriaga, A. B.; Goldschmidt, L.; Flot, D.; Cascio, D.; Sawaya, M. R.; Eisenberg, D. Molecular Basis for Amyloid-Beta Polymorphism. *Proc. Natl. Acad. Sci. U. S. A.* **2011**, *108* (41), 16938−16943.

(12) Iadanza, M. G.; Jackson, M. P.; Hewitt, E. W.; Ranson, N. A.; Radford, S. E. A New Era for Understanding Amyloid Structures and Disease. *Nat. Rev. Mol. Cell Biol.* **2018**, *19*, 755−773.

(13) Rasmussen, J.; Mahler, J.; Beschorner, N.; Kaeser, S. A.; Häsler, L. M.; Baumann, F.; Nyström, S.; Portelius, E.; Blennow, K.; Lashley, T.; Fox, N.; Sepulveda-Falla, D.; Glatzel, M.; Oblak, A. L.; Ghetti, B.; Nilsson, K. P. R.; Hammarstrom, P.; Staufenbiel, M.; Walker, L. C.; Jucker, M. Amyloid Polymorphisms Constitute Distinct Clouds of Conformational Variants in Different Etiological Subtypes of Alzheimer's Disease. *Proc. Natl. Acad. Sci. U. S. A.* **2017**, *114* (49), 13018−13023.

(14) Ghosh, R.; Dong, J.; Wall, J.; Frederick, K. K. Amyloid Fibrils Embodying Distinctive Yeast Prion Phenotypes Exhibit Diverse Morphologies. *FEMS Yeast Res.* **2018**, *18* (6), foy059.

(15) Zhang, W.; Tarutani, A.; Newell, K. L.; Murzin, A. G.; Matsubara, T.; Falcon, B.; Vidal, R.; Garringer, H. J.; Shi, Y.; Ikeuchi, T.; Murayama, S.; Ghetti, B.; Goedert, M.; Scheres, S.; Hasegawa, M. Novel Tau Filament Fold in Corticobasal Degeneration. *Nature* **2020**, *580*, 283−287.

(16) Zhang, W.; Falcon, B.; Murzin, A. G.; Fan, J.; Crowther, R. A.; Goedert, M.; Scheres, S. H. W. Heparin-Induced Tau Filaments Are

Polymorphic and Differ from Those in Alzheimer's and Pick's Diseases. *eLife* **2019**, *8*, e43584.

(17) Berry, D. B.; Lu, D.; Geva, M.; Watts, J. C.; Bhardwaj, S.; Oehler, A.; Renslo, A. R.; Dearmond, S. J.; Prusiner, S. B.; Giles, K. Drug Resistance Confounding Prion Therapeutics. *Proc. Natl. Acad. Sci. U. S. A.* **2013**, *110* (44), E4160–E4169.

(18) Tycko, R. Physical and Structural Basis for Polymorphism in Amyloid Fibrils. *Protein Sci.* **2014**, *23* (11), 1528–1539.

(19) Paravastu, A. K.; Leapman, R. D.; Yau, W. M.; Tycko, R. Molecular Structural Basis for Polymorphism in Alzheimer's β-Amyloid Fibrils. *Proc. Natl. Acad. Sci. U. S. A.* **2008**, *105* (47), 18349–18354.

(20) Salveson, P. J.; Spencer, R. K.; Kreutzer, A. G.; Nowick, J. S. X-Ray Crystallographic Structure of a Compact Dodecamer from a Peptide Derived from Aβ16–36. *Org. Lett.* **2017**, *19* (13), 3462–3465.

(21) Kreutzer, A. G.; Hamza, I. L.; Spencer, R. K.; Nowick, J. S. X-Ray Crystallographic Structures of a Trimer, Dodecamer, and Annular Pore Formed by an Aβ17–36 β-Hairpin. *J. Am. Chem. Soc.* **2016**, *138* (13), 4634–4642.

(22) Serpell, L. C. Alzheimer's Amyloid Fibrils: Structure and Assembly. *Biochim. Biophys. Acta, Mol. Basis Dis.* **2000**, *1502*, 16–30.

(23) Boyer, D. R.; Li, B.; Sun, C.; Fan, W.; Sawaya, M. R.; Jiang, L.; Eisenberg, D. S. Structures of Fibrils Formed by α-Synuclein Hereditary Disease Mutant H50Q Reveal New Polymorphs. *Nat. Struct. Mol. Biol.* **2019**, *26*, 1044–1052.

(24) Kollmer, M.; Close, W.; Funk, L.; Rasmussen, J.; Bsoul, A.; Schierhorn, A.; Schmidt, M.; Sigurdson, C. J.; Jucker, M.; Fändrich, M. Cryo-EM Structure and Polymorphism of Aβ Amyloid Fibrils Purified from Alzheimer's Brain Tissue. *Nat. Commun.* **2019**, *10* (1), 4760.

(25) Lippens, G.; Gigant, B. Elucidating Tau Function and Dysfunction in the Era of Cryo-EM. *J. Biol. Chem.* **2019**, *294*, 9316–9325.

(26) Boyer, D. R.; Li, B.; Sun, C.; Fan, W.; Sawaya, M. R.; Jiang, L.; Eisenberg, D. S. Structures of Fibrils Formed by α-Synuclein Hereditary Disease Mutant H50Q Reveal New Polymorphs. *Nat. Struct. Mol. Biol.* **2019**, *26*, 1044–1052.

(27) Meinhardt, J.; Sachse, C.; Hortschansky, P.; Grigorieff, N.; Fändrich, M. Aβ(1–40) Fibril Polymorphism Implies Diverse Interaction Patterns in Amyloid Fibrils. *J. Mol. Biol.* **2009**, *386* (3), 869–877.

(28) Tycko, R. Amyloid Polymorphism: Structural Basis and Neurobiological Relevance. *Neuron* **2015**, *86* (3), 632–645.

(29) Lu, J. X.; Qiang, W.; Yau, W. M.; Schwieters, C. D.; Meredith, S. C.; Tycko, R. XMolecular Structure of β-Amyloid Fibrils in Alzheimer's Disease Brain Tissue. *Cell* **2013**, *154* (6), 1257.

(30) Lee, J.; Culyba, E. K.; Powers, E. T.; Kelly, J. W. Amyloid-β Forms Fibrils by Nucleated Conformational Conversion of Oligomers. *Nat. Chem. Biol.* **2011**, *7* (9), 602–609.

(31) Bunce, S. J.; Wang, Y.; Stewart, K. L.; Ashcroft, A. E.; Radford, S. E.; Hall, C. K.; Wilson, A. J. Molecular Insights into the Surface-Catalyzed Secondary Nucleation of Amyloid-40 (A40) by the Peptide Fragment A16–22. *Sci. Adv.* **2019**, *5* (6), eaav8216.

(32) Morel, B.; Varela, L.; Azuaga, A. I.; Conejero-Lara, F. Environmental Conditions Affect the Kinetics of Nucleation of Amyloid Fibrils and Determine Their Morphology. *Biophys. J.* **2010**, *99* (11), 3801–3810.

(33) Cohen, S. I. A.; Linse, S.; Luheshi, L. M.; Hellstrand, E.; White, D. A.; Rajah, L.; Otzen, D. E.; Vendruscolo, M.; Dobson, C. M.; Knowles, T. P. J. Proliferation of Amyloid-Β42 Aggregates Occurs through a Secondary Nucleation Mechanism. *Proc. Natl. Acad. Sci. U. S. A.* **2013**, *110* (24), 9758–9763.

(34) Månsson, C.; Arosio, P.; Hussein, R.; Kampinga, H. H.; Hashem, R. M.; Boelens, W. C.; Dobson, C. M.; Knowles, T. P. J.; Linse, S.; Emanuelsson, C. Interaction of the Molecular Chaperone DNAJB6 with Growing Amyloid-Beta 42 (Aβ42) Aggregates Leads to Sub-Stoichiometric Inhibition of Amyloid Formation. *J. Biol. Chem.* **2014**, *289* (45), 31066–31076.

(35) Arosio, P.; Michaels, T. C. T.; Linse, S.; Månsson, C.; Emanuelsson, C.; Presto, J.; Johansson, J.; Vendruscolo, M.; Dobson, C. M.; Knowles, T. P. J. Kinetic Analysis Reveals the Diversity of Microscopic Mechanisms through Which Molecular Chaperones Suppress Amyloid Formation. *Nat. Commun.* **2016**, *7*, 10948.

(36) Liu, Y.; Nguyen, M.; Robert, A.; Meunier, B. Metal Ions in Alzheimer's Disease: A Key Role or Not? *Acc. Chem. Res.* **2019**, *52* (7), 2026–2035.

(37) Lee, M.; Kim, J. I.; Na, S.; Eom, K. Metal Ions Affect the Formation and Stability of Amyloid β Aggregates at Multiple Length Scales. *Phys. Chem. Chem. Phys.* **2018**, *20* (13), 8951–8961.

(38) Serra-Batiste, M.; Ninot-Pedrosa, M.; Bayoumi, M.; Gairí, M.; Maglia, G.; Carulla, N. Aβ42 Assembles into Specific β-Barrel Pore-Forming Oligomers in Membrane-Mimicking Environments. *Proc. Natl. Acad. Sci. U. S. A.* **2016**, *113* (39), 10866–10871.

(39) Han, S.; Kollmer, M.; Markx, D.; Claus, S.; Walther, P.; Fändrich, M. Amyloid Plaque Structure and Cell Surface Interactions of β-Amyloid Fibrils Revealed by Electron Tomography. *Sci. Rep.* **2017**, *7*, 43577.

(40) Chatani, E.; Yamamoto, N. Recent Progress on Understanding the Mechanisms of Amyloid Nucleation. *Biophys. Rev.* **2018**, *10*, 527–534.

(41) Zhang, L.; Schmit, J. D. Theory of Amyloid Fibril Nucleation from Folded. *Isr. J. Chem.* **2017**, *57* (7), 738–749.

(42) Törnquist, M.; Michaels, T. C. T.; Sanagavarapu, K.; Yang, X.; Meisl, G.; Cohen, S. I. A.; Knowles, T. P. J.; Linse, S. Secondary Nucleation in Amyloid Formation. *Chem. Commun.* **2018**, *54* (63), 8667–8684.

(43) Petkova, A. T.; Leapman, R. D.; Guo, Z.; Yau, W. M.; Mattson, M. P.; Tycko, R. Self-Propagating, Molecular-Level Polymorphism in Alzheimer's β-Amyloid Fibrils. *Science* **2005**, *307* (5707), 262–265.

(44) Morozova, O. A.; March, Z. M.; Robinson, A. S.; Colby, D. W. Conformational Features of Tau Fibrils from Alzheimer's Disease Brain Are Faithfully Propagated by Unmodified Recombinant Protein. *Biochemistry* **2013**, *52* (40), 6960–6967.

(45) Lucas, M. J.; Keitz, B. K. Influence of Zeolites on Amyloid-β Aggregation. *Langmuir* **2018**, *34* (33), 9789–9797.

(46) Moore, K. A.; Pate, K. M.; Soto-Ortega, D.; Lohse, S.; van der Munnik, N.; Lim, M.; Jackson, K. S.; Lyles, V. D.; Jones, L.; Glassgow, N.; Napumecheno, V.; Mobley, S.; Uline, M.; Mahtab, R.; Murphy, C.; Moss, M. Influence of Gold Nanoparticle Surface Chemistry and Diameter upon Alzheimer's Disease Amyloid-β Protein Aggregation. *J. Biol. Eng.* **2017**, *11* (1), 5.

(47) Song, Y.; Moore, E. G.; Guo, Y.; Moore, J. S. Polymer-Peptide Conjugates Disassemble Amyloid β Fibrils in a Molecular-Weight Dependent Manner. *J. Am. Chem. Soc.* **2017**, *139* (12), 4298–4301.

(48) Sahoo, B. R.; Genjo, T.; Bekier, M.; Cox, S. J.; Stoddard, A. K.; Ivanova, M.; Yasuhara, K.; Fierke, C. A.; Wang, Y.; Ramamoorthy, A. Alzheimer's Amyloid-Beta Intermediates Generated Using Polymer-Nanodiscs. *Chem. Commun. (Cambridge, U. K.)* **2018**, *54* (91), 12883–12886.

(49) Linse, S.; Cabaleiro-Lago, C.; Xue, W.-F.; Lynch, I.; Lindman, S.; Thulin, E.; Radford, S. E.; Dawson, K. A. Nucleation of Protein Fibrillation by Nanoparticles. *Proc. Natl. Acad. Sci. U. S. A.* **2007**, *104* (21), 8691–8696.

(50) Rahimi, F.; Maiti, P.; Bitan, G. Photo-Induced Cross-Linking of Unmodified Proteins (PICUP) Applied to Amyloidogenic Peptides. *J. Visualized Exp.* **2009**, No. 23, e1071.

(51) Tang, G.; Peng, L.; Baldwin, P. R.; Mann, D. S.; Jiang, W.; Rees, I.; Ludtke, S. J. EMAN2: An Extensible Image Processing Suite for Electron Microscopy. *J. Struct. Biol.* **2007**, *157* (1), 38–46.

(52) Ulrich, K.; Galvosas, P.; Kärger, J.; Grinberg, F.; Vernimmen, J.; Meynen, V.; Cool, P. Self-Assembly and Diffusion of Block Copolymer Templates in SBA-15 Nanochannels. *J. Phys. Chem. B* **2010**, *114* (12), 4223–4229.

(53) Huirache-Acuña, R.; Nava, R.; Peza-Ledesma, C.; Lara-Romero, J.; Alonso-Núez, G.; Pawelec, B.; Rivera-Muñoz, E. SBA-15 Mesoporous Silica as Catalytic Support for Hydrodesulfurization Catalysts—Review. *Materials* **2013**, *6* (9), 4139–4167.

(54) Hamilton, B. D.; Ha, J. M.; Hillmyer, M. A.; Ward, M. D. Manipulating Crystal Growth and Polymorphism by Confinement in Nanoscale Crystallization Chambers. *Acc. Chem. Res.* **2012**, *45* (3), 414−423.

(55) Ha, J. M.; Wolf, J. H.; Hillmyer, M. A.; Ward, M. D. Polymorph Selectivity under Nanoscopic Confinement. *J. Am. Chem. Soc.* **2004**, *126* (11), 3382−3383.

(56) Lynch, M. M.; Liu, J.; Nigra, M.; Coppens, M. O. Chaperonin-Inspired PH Protection by Mesoporous Silica SBA-15 on Myoglobin and Lysozyme. *Langmuir* **2016**, *32* (37), 9604−9610.

(57) Siefker, J.; Biehl, R.; Kruteva, M.; Feoktystov, A.; Coppens, M. O. Confinement Facilitated Protein Stabilization As Investigated by Small-Angle Neutron Scattering. *J. Am. Chem. Soc.* **2018**, *140* (40), 12720−12723.

(58) Chaudhary, V.; Sharma, S. An Overview of Ordered Mesoporous Material SBA-15: Synthesis, Functionalization and Application in Oxidation Reactions. *J. Porous Mater.* **2017**, *24* (3), 741−749.

(59) Cheignon, C.; Tomas, M.; Bonnefont-Rousselot, D.; Faller, P.; Hureau, C.; Collin, F. Oxidative Stress and the Amyloid Beta Peptide in Alzheimer's Disease. *Redox Biol.* **2018**, *14*, 450−464.

(60) Strittmatter, W. J.; Weisgraber, K. H.; Huang, D. Y.; Dong, L. M.; Salvesen, G. S.; Pericak-Vance, M.; Schmechel, D.; Saunders, A. M.; Goldgaber, D.; Roses, A. D. Binding of Human Apolipoprotein E to Synthetic Amyloid β Peptide: Isoform-Specific Effects and Implications for Late-Onset Alzheimer Disease. *Proc. Natl. Acad. Sci. U. S. A.* **1993**, *90* (17), 8098−8102.

(61) Jarosz-Griffiths, H. H.; Noble, E.; Rushworth, J. V.; Hooper, N. M. Amyloid-β Receptors: The Good, the Bad, and the Prion Protein. *J. Biol. Chem.* **2016**, *291*, 3174−3183.

(62) Gobbi, M.; Re, F.; Canovi, M.; Beeg, M.; Gregori, M.; Sesana, S.; Sonnino, S.; Brogioli, D.; Musicanti, C.; Gasco, P.; Salmona, M.; Masserini, M. Lipid-Based Nanoparticles with High Binding Affinity for Amyloid-B1−42 Peptide. *Biomaterials* **2010**, *31* (25), 6519−6529.

(63) Chen, G. F.; Xu, T. H.; Yan, Y.; Zhou, Y. R.; Jiang, Y.; Melcher, K.; Xu, H. E. Amyloid Beta: Structure, Biology and Structure-Based Therapeutic Development. *Acta Pharmacol. Sin.* **2017**, *38*, 1205−1235.

(64) Viet, M. H.; Ngo, S. T.; Lam, N. S.; Li, M. S. Inhibition of Aggregation of Amyloid Peptides by Beta-Sheet Breaker Peptides and Their Binding Affinity. *J. Phys. Chem. B* **2011**, *115* (22), 7433−7446.

(65) Biancalana, M.; Koide, S. Molecular Mechanism of Thioflavin-T Binding to Amyloid Fibrils. *Biochim. Biophys. Acta, Proteins Proteomics* **2010**, *1804* (7), 1405−1412.

(66) Arosio, P.; Knowles, T. P. J.; Linse, S. On the Lag Phase in Amyloid Fibril Formation. *Phys. Chem. Chem. Phys.* **2015**, *17* (12), 7606−7618.

(67) Hellstrand, E.; Boland, B.; Walsh, D. M.; Linse, S. Amyloid Beta-Protein Aggregation Produces Highly Reproducible Kinetic Data and Occurs by a Two-Phase Process. *ACS Chem. Neurosci.* **2010**, *1* (1), 13−18.

(68) Accardo, A.; Shalabaeva, V.; Di Cola, E.; Burghammer, M.; Krahne, R.; Riekel, C.; Dante, S. Superhydrophobic Surfaces Boost Fibril Self-Assembly of Amyloid β Peptides. *ACS Appl. Mater. Interfaces* **2015**, *7* (37), 20875−20884.

(69) Vugmeyster, L.; Clark, M. A.; Falconer, I. B.; Ostrovsky, D.; Gantz, D.; Qiang, W.; Hoatson, G. L. Flexibility and Solvation of Amyloid-β Hydrophobic Core. *J. Biol. Chem.* **2016**, *291* (35), 18484−18495.

(70) Qiang, W.; Yau, W. M.; Luo, Y.; Mattson, M. P.; Tycko, R. Antiparallel β-Sheet Architecture in Iowa-Mutant β-Amyloid Fibrils. *Proc. Natl. Acad. Sci. U. S. A.* **2012**, *109* (12), 4443−4448.

(71) Cerf, E.; Sarroukh, R.; Tamamizu-Kato, S.; Breydo, L.; Derclaye, S.; Dufrêne, Y. F.; Narayanaswami, V.; Goormaghtigh, E.; Ruysschaert, J. M.; Raussens, V. Antiparallel β-Sheet: A Signature Structure of the Oligomeric Amyloid β-Peptide. *Biochem. J.* **2009**, *421* (3), 415−423.

(72) Watanabe-Nakayama, T.; Ono, K.; Itami, M.; Takahashi, R.; Teplow, D. B.; Yamada, M. High-Speed Atomic Force Microscopy Reveals Structural Dynamics of Amyloid β 1−42 Aggregates. *Proc. Natl. Acad. Sci. U. S. A.* **2016**, *113* (21), 5835−5840.

(73) Usov, I.; Adamcik, J.; Mezzenga, R. Polymorphism Complexity and Handedness Inversion in Serum Albumin Amyloid Fibrils. *ACS Nano* **2013**, *7* (12), 10465−10474.

(74) Ezzat, K.; Pernemalm, M.; Pålsson, S.; Roberts, T. C.; Järver, P.; Dondalska, A.; Bestas, B.; Sobkowiak, M. J.; Levänen, B.; Sköld, M.; Thompson, E.; Saher, O.; Kari, O.; Lajunen, T.; Ekstrom, E. S.; Nilsson, C.; Ishchenko, Y.; Malm, T.; Wood, M.; Power, U. F.; Masich, S.; Linden, A.; Sandberg, J. K.; Lehtio, J.; Spetz, A. L.; EL Andaloussi, S. The Viral Protein Corona Directs Viral Pathogenesis and Amyloid Aggregation. *Nat. Commun.* **2019**, *10* (1), 2331.

(75) Schmidt, M.; Sachse, C.; Richter, W.; Xu, C.; Fändrich, M.; Grigorieff, N. Comparison of Alzheimer Aβ(1−40) and Aβ(1−42) Amyloid Fibrils Reveals Similar Protofilament Structures. *Proc. Natl. Acad. Sci. U. S. A.* **2009**, *106* (47), 19813−19818.

(76) Scheres, S. H. W. RELION: Implementation of a Bayesian Approach to Cryo-EM Structure Determination. *J. Struct. Biol.* **2012**, *180* (3), 519−530.

(77) Rangachari, V.; Moore, B. D.; Reed, D. K.; Sonoda, L. K.; Bridges, A. W.; Conboy, E.; Hartigan, D.; Rosenberry, T. L. Amyloid-β(1−42) Rapidly Forms Protofibrils and Oligomers by Distinct Pathways in Low Concentrations of Sodium Dodecylsulfate. *Biochemistry* **2007**, *46* (43), 12451−12462.

(78) Mitchell, C. A.; Yu, L.; Ward, M. D. Selective Nucleation and Discovery of Organic Polymorphs through Epitaxy with Single Crystal Substrates. *J. Am. Chem. Soc.* **2001**, *123* (44), 10830−10839.

(79) Klement, K.; Wieligmann, K.; Meinhardt, J.; Hortschansky, P.; Richter, W.; Fändrich, M. Effect of Different Salt Ions on the Propensity of Aggregation and on the Structure of Alzheimer's Aβ(1−40) Amyloid Fibrils. *J. Mol. Biol.* **2007**, *373* (5), 1321−1333.

(80) Schmidt, M.; Sachse, C.; Richter, W.; Xu, C.; Fandrich, M.; Grigorieff, N. Comparison of Alzheimer A (1−40) and A (1−42) Amyloid Fibrils Reveals Similar Protofilament Structures. *Proc. Natl. Acad. Sci. U. S. A.* **2009**, *106* (47), 19813−19818.

(81) Periole, X.; Rampioni, A.; Vendruscolo, M.; Mark, A. E. Factors That Affect the Degree of Twist in β-Sheet Structures: A Molecular Dynamics Simulation Study of a Cross-β Filament of the GNNQQNY Peptide. *J. Phys. Chem. B* **2009**, *113* (6), 1728−1737.

(82) Periole, X.; Huber, T.; Bonito-Oliva, A.; Aberg, K. C.; Van Der Wel, P. C. A.; Sakmar, T. P.; Marrink, S. J. Energetics Underlying Twist Polymorphisms in Amyloid Fibrils. *J. Phys. Chem. B* **2018**, *122* (3), 1081−1091.

(83) Eisenberg, D.; Schwarz, E.; Komaromy, M.; Wall, R. Analysis of Membrane and Surface Protein Sequences with the Hydrophobic Moment Plot. *J. Mol. Biol.* **1984**, *179* (1), 125−142.

(84) Hu, Z. W.; Vugmeyster, L.; Au, D. F.; Ostrovsky, D.; Sun, Y.; Qiang, W. Molecular Structure of an N-Terminal Phosphorylated β-Amyloid Fibril. *Proc. Natl. Acad. Sci. U. S. A.* **2019**, *116* (23), 11253−11258.

(85) Arakhamia, T.; Lee, C. E.; Carlomagno, Y.; Duong, D. M.; Kundinger, S. R.; Wang, K.; Williams, D.; DeTure, M.; Dickson, D. W.; Cook, C. N.; Seyfried, N. T.; Petrucelli, L.; Fitzpatrick, A. Posttranslational Modifications Mediate the Structural Diversity of Tauopathy Strains. *Cell* **2020**, *180* (4), 633−644.e12.